A Nonmodal Instability Perspective of the Declining Northern Midlatitude Synoptic Variability in Boreal Summer

SIYU ZHAO AND YI DENG

School of Earth and Atmospheric Sciences, Georgia Institute of Technology, Atlanta, Georgia

WENHONG LI

Earth and Ocean Sciences, Nicholas School, Duke University, Durham, North Carolina

(Manuscript received 20 November 2018, in final form 8 October 2019)

ABSTRACT

The Pacific–North America–North Atlantic sector in general experienced a dryer and warmer climate in summer during the past 40 years. These changes are partly associated with declining midlatitude synoptic variability in boreal summer, especially over the two ocean basins. A nonmodal instability analysis of the boreal summer background flow is conducted for two periods, 1979–94 and 2000–15, to understand dynamical processes potentially responsible for the observed decline of synoptic variability. The synoptic variability associated with fast, nonmodal growth of atmospheric disturbances shows a decline over northern midlatitudes in the later period, in both a barotropic model and a two-level quasigeostrophic model. These results highlight the importance of the changing summer background flow in contributing to the observed changes in synoptic variability. Also discussed are factors likely associated with background flow changes including sea surface temperature and sea ice change.

1. Introduction

The changing climate has profound impacts on human life, health, and socioeconomic well-being. The manifestation of climate change is not only rising global-mean temperature, but also regional changes in floods, droughts, storminess, heat/cold waves, and wildfires (Xie et al. 2015). Numerous studies have documented increasing probabilities in the occurrence of weather extremes in association with ongoing global climate change (e.g., Groisman et al. 1999, 2005; Westra et al. 2013). It is shown that the frequency and intensity of extreme heat and precipitation events have largely increased since the late 1980s, especially over the midlatitudes (e.g., Fischer and Knutti 2015; Lehmann et al. 2015). Dai (2013) observed an increasing trend of global-mean aridity measured in self-calibrated Palmer drought severity index from 1923 to 2010 and argued that severe drought condition may continue in the future due to either decreased precipitation and/or increased evaporation. In fact, changes in precipitation vary strongly across geographical locations (e.g., Donat et al. 2016). Lehmann et al. (2018) found that there is increased occurrence of record-wet months in the global mean, especially over northern middle to high latitudes, while varying trends have been detected over tropics. Held and Soden (2006) suggested that wet regions may get wetter and dry regions may get drier due to the effects of evaporation and precipitation. Global climate models have been widely applied to simulate the observed trends (e.g., Thorne et al. 2015). Specifically, the trend in global-mean surface temperature is well captured by model simulations, but substantial differences are found in regional surface temperature trends (Lin and Huybers 2016). A thorough understanding of the dynamics and physics linked to these changes is crucial for assessing a wide range of detrimental impacts including water supply deficiency, decreased crop yields, rising food prices, and increased wildfires.

In northern midlatitudes, it was observed that many weather extremes including severe droughts and heat extremes occurred during recent boreal summer (e.g., Petoukhov et al. 2016; Kornhuber et al. 2019). During 2012–14, California experienced record-breaking droughts, leading to large amount of agricultural and ecological losses (Williams et al. 2015). In 2010, Russia suffered

Corresponding author: Yi Deng, yi.deng@eas.gatech.edu

DOI: 10.1175/JCLI-D-18-0799.1

both heat wave and drought, resulting in 500 wildfires around Moscow and 30% grain-harvest losses (Coumou and Rahmstorf 2012). The large damage caused by the combined effect of heat extremes and dryness is due to strong anticorrelation between temperature and precipitation during summer over the extratropics (Coumou et al. 2018). It is known that both thermodynamic and dynamic factors contribute to the summer compound extremes (i.e., heat wave and dryness). In terms of the thermodynamic effect, soil moisture plays an important role in modulating local weather. For example, a strong correlation is found among precipitation, soil moisture, and convective inhibition (Myoung and Nielsen-Gammon 2010). Such correlation includes both the impacts of precipitation on soil moisture and the feedbacks of soil moisture on precipitation through convective inhibition. Soil moisture–climate interactions also have significant impacts on heat wave due to the presence or lack of evaporative cooling (e.g., Lorenz et al. 2010; Jaeger and Seneviratne 2011).

In addition, atmospheric dynamic factors may also trigger and sustain heat waves and droughts. In the past 40 years, a weakening summer circulation (on synoptic scales) associated with rapid Arctic warming was observed in northern midlatitudes (e.g., Coumou et al. 2015), accompanied by more persistent heat waves in recent summers (e.g., Pfleiderer and Coumou 2018). As suggested by their paper, in a typical summer, synoptic disturbances transport moist and cool air from oceans to continents, reducing heat and dry conditions. However, low synoptic activity and associated low eddy kinetic energy (EKE) will lead to less frequent cool maritime air masses, creating favorable conditions for the buildup of heat waves and drought over continents (Lehmann and Coumou 2015). Chang et al. (2016) suggested that decrease in extratropical cyclone activity can result in decrease in cloud cover, thus favoring higher temperature. Brewer and Mass (2016a,b) showed that heat waves over the western United States are impacted by synoptic variability, which may change the amplitude and frequency of offshore flow. Coumou et al. (2015) argued that the weakening of summer circulation in recent decades could be attributed to 1) weakening of zonal wind (westerly jet) by a reduction in the poleward temperature gradient and 2) changes in the amplitude of Rossby waves and EKE. Previous studies have suggested that the westerly jet can act as a waveguide and produce zonally oriented chains of perturbations, of which those near the jet core will be refracted toward the core (e.g., Branstator 2002). Hoskins and Ambrizzi (1993) defined the location of local maximum stationary wavenumber K_s as a Rossby waveguide and found that during winter a waveguide with typical stationary wavenumber 7 (5) occurs along with the Asian (North Atlantic) jet.

During boreal summer, a circumglobal teleconnection (CGT) pattern with a zonal wavenumber-5 structure is embedded in the summer jet, being a major source of climate variability and predictability in the midlatitude regions (e.g., Ding and Wang 2005; Wang et al. 2012; Teng et al. 2013). The CGT pattern can generate local weather extremes (e.g., heat waves) through the downstream effect of Rossby wave. In addition to the global-scale CGT pattern, previous studies have also focused on the large-scale meteorological pattern ($\sim 10^3$ km) over the Pacific–North America sector. Li et al. (2014) investigated the influences of the Pacific–Japan (PJ) teleconnection pattern, which is characterized by an extratropical wave train on synoptic scales over the western Pacific. It is found that the positive (negative) PJ phase strengthens (weakens) the synoptic variability over the western North Pacific. Such a summer wave train pattern over the North Pacific has also been identified in some other studies. For example, anomalous heating over East Asia can influence summer hydroclimate over North America via generating an upper-level Rossby wave train. In the papers by Zhu and Li (2016) and Zhao et al. (2018), the time scale of the initial disturbances traveling from East Asia to North America ranges from several days to 1 month.

Based on previous studies discussed above, the waveguide and wave train pattern play a significant role in triggering the midlatitude weather extremes. However, some issues remain unaddressed, especially those related to the connections between time-mean circulation change and short-time weather change. To understand such connections, one route is to investigate changes in the instability properties of a background "time-mean" flow where the instability being examined is believed to be responsible for spontaneous growth of weather disturbances. Previous studies have applied both modal (associated with one normal mode) and nonmodal (associated with growth comprising more than one normal mode) instability analysis to understand the growth of disturbance. Simmons et al. (1983) showed that low-frequency oscillation such as the Pacific–North American pattern is probably linked to the most rapidly growing normal mode of observed wintertime-mean flows. Hall and Sardeshmukh (1998) also found that the fastest growing normal mode resembles the observed wave train in midlatitudes.

Nonmodal instability analysis (NIA) has been widely applied to basic flows (either barotropic or baroclinic) to examine excitation and growth of perturbations (e.g., Farrell 1988, 1989; Mak and Cai 1989; Huang 1999; Hakim 2000; Stevens and Hakim 2005; Wolfe and

Samelson 2008). A disturbance that accumulatively intensifies the most over a specific time interval is named as an ''optimal mode'' in contrast to the unstable normal modes in the modal instability analysis (Mak 2011a,b). Chang and Mak (1995) investigated the nonmodal growth of observed intraseasonal disturbances of winter-mean flows and found that the most pronounced optimal mode with 1-day optimization time (i.e., intensifying the most in 1 day) has a characteristic time scale of 20 days and locates over the Atlantic. Borges and Hartmann (1992) demonstrated, in a divergent barotropic model with the 1985/86 winter flow, that optimal perturbations become more localized when the optimization time becomes smaller. The dynamics of winter storm tracks was studied from a linear instability perspective and a large number of optimal modes with optimization time up to 10 days were found in the midlatitudes (Lee and Mak 1995). It is interesting to note that the concept of ''optimal growth'' was also used to investigate the growth and evolution of El Niño–Southern Oscillation (ENSO) events (e.g., Newman et al. 2011; Vimont et al. 2014), where the initial conditions characterized by sea surface temperature (SST) and thermocline anomalies are found to be important in triggering different types of ENSO events. Most recently, Zhao et al. (2018) applied the NIA to the summer climatological flow and found that one of the top optimal modes resembles an intraseasonal mode of atmospheric variability in the midlatitudes. This optimal mode grows from an initial disturbance over East Asia and attains its maximum amplitude around 9 days.

Given the role of nonmodal instability in the excitation of synoptic-scale disturbances, here we try to understand the changing climate in northern midlatitudes, characterized by the decline of synoptic variability in recent decades, in the context of changing instability properties of the summer background flow. We first identify the changes in midlatitude summer precipitation and near-surface temperature during the past 40 years. The role of the background flow and synoptic disturbances in such changes will be investigated by applying the NIA to the observed summer background flow in both a barotropic model and a two-level quasigeostrophic (QG) model.

2. Data and methodology

a. Data

The observed monthly mean precipitation rate used in this study is from the Global Precipitation Climatology Project (GPCP), at the resolution of 2.5° in both longitude and latitude (Adler et al. 2003). This study also uses the daily mean geopotential height and zonal and meridional winds from the National Centers for Environmental Prediction (NCEP)–National Center for Atmospheric Research (NCAR) reanalysis (Kalnay et al. 1996), with the same horizontal resolution as the GPCP data. The daily mean 2-m temperature with a Gaussian grid is also from the NCEP–NCAR reanalysis. The results among different reanalysis datasets are expected to be very similar since we study the long-term change of the climate in this paper. We have especially examined the ERA-Interim data for 2-m temperature (Dee et al. 2011). The results obtained from the ERA-Interim are all qualitatively similar to those obtained from the NCEP–NCAR reanalysis. The monthly mean SST and sea ice concentration (SIC) come from the Hadley Centre Sea Ice and Sea Surface Temperature datasets (HadISST) at a resolution of 1.0° in both longitude and latitude (Rayner et al. 2003). The AMO index is available at https://www.esrl.noaa.gov/psd/data/timeseries/AMO/. The PDO index is available at https://www.ncdc.noaa.gov/teleconnections/pdo/. The analyses cover boreal summer (June–August) for the period 1979–2015.

b. Statistical analysis

In this study, the early and late periods are defined as 1979–94 and 2000–15, respectively, since 1995–99 is expected to be a transition period for some low-frequency modes of climate variability such as Pacific decadal oscillation (PDO) and Atlantic multidecadal oscillation (AMO) (e.g., Dai 2013; Stolpe et al. 2017). The composite anomalies for the early or late period are calculated by subtracting the summer climatology from the average of the annual-mean data over that period. The Student's t test is applied to examine the significance of composite anomalies.

This study also measures summer heat waves over East Asia (30°–50°N, 100°–120°E) and western North America (30°–50°N, 100°–125°W), respectively. Similar to the detection of hydrological extremes in Zhao et al. (2016, 2017a), anomalous hot days are first defined at each grid point in the following manner: if the daily 2-m temperature at the grid point exceeds the 90th percentile for the calendar day over the period 1979–2015, we classify that day as an anomalous hot day. This classification is performed for all days (1979–2015) and each grid point over the selected domain. To identify heat waves having a large regional impact, we additionally require that for any single day the number of grid points exceeding the anomalous hot day threshold must exceed 20% of the total number of grid points in that domain. Such days are classified as

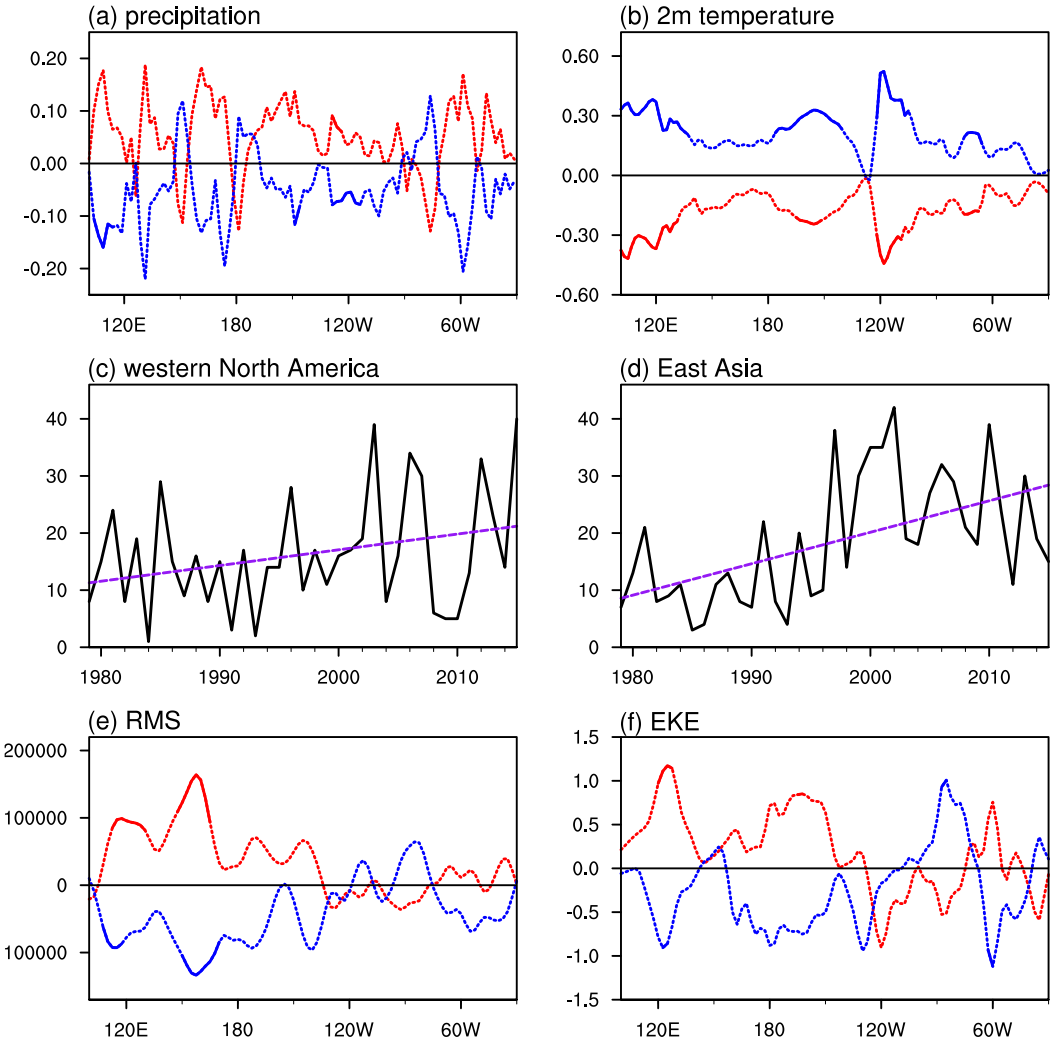

FIG. 1. (a) The 30°–50°N-averaged summer-mean precipitation anomaly (mm day^{-1}) averaged for the early (red line) and late period (blue line) over 100°E–30°W. Solid lines are significant at the 0.05 level. (b) As in (a), but for the 2-m temperature (°C). (c) Summer heat wave days averaged over the western North America during 1979–2015 (solid line). Dashed line is the long-term trend. (d) As in (c), but for East Asia. (e),(f) As in (a), but for RMS of 2.5–6-day bandpass-filtered 250 hPa streamfunction (m^2 s^{-1}) and EKE (m^2 s^{-2}), respectively.

heat wave days. Finally, the seasonal total number of heat wave days is computed for each year. The results obtained for the yearly (summer) hot wave days from sensitivity experiments (by adjusting detection thresholds) are all qualitatively similar to those presented in section 3.

The maximum covariance analysis (MCA) has been widely used to isolate linear covarying (coupled) patterns between two geophysical fields (e.g., Bretherton et al. 1992; Czaja and Frankignoul 2002; Hartmann 2016). In this study, we apply the MCA to the undetrended (detrended) seasonal-mean 250-hPa streamfunction anomaly over the Northern Hemisphere (10°–70°N, 0°–360°) paired with the undetrended (detrended) seasonal-mean SST anomaly (20°–70°N, 0°–360°) and SIC anomaly (60°–90°N, 0°–360°), respectively. To reduce the impact of high-latitude grid points, we apply an area weight (taking the square root of the cosine of latitude) for the data before the MCA.

c. *Nonmodal instability analysis using a barotropic model*

Following Zhao et al. (2018), we apply the NIA for the barotropic model to obtain disturbances accumulatively intensifying the *most* over a time interval τ. We first compute normal modes associated with the background flow by applying the linearized unforced nondivergent barotropic vorticity equation in spherical

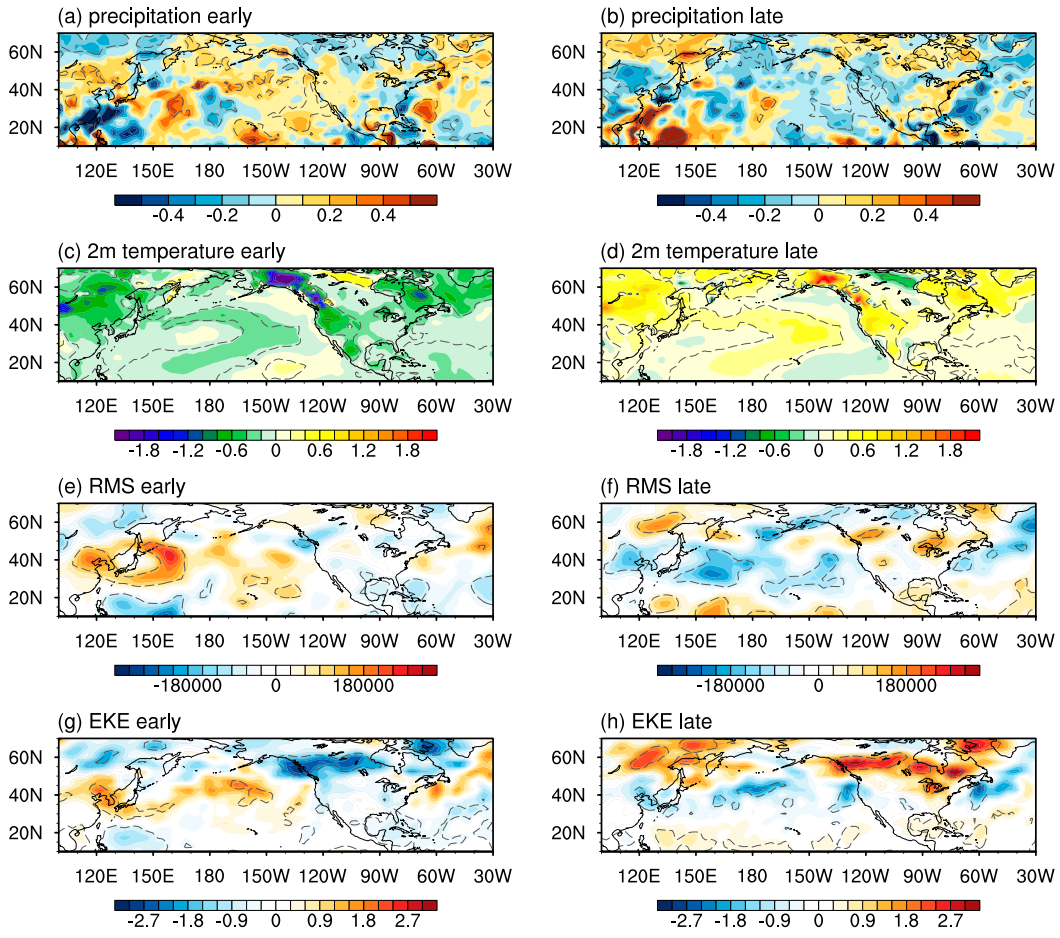

FIG. 2. (a) The summer-mean precipitation anomaly (mm day^{-1}) averaged for the early period. (b) As in (a), but for the late period. (c),(e),(g) As in (a), but for 2-m temperature (°C), RMS of 2.5–6-day bandpass-filtered 250-hPa streamfunction (m^2 s^{-1}), and EKE (m^2 s^{-2}), respectively. (d),(f),(h) As in (c), (e), and (g), but for the late period. Contours are significant at the 0.05 level.

coordinates [Eq. (4) in Zhao et al. (2018) with a damping term ($-\kappa\nabla^2\psi'$) on the rhs; κ is the frictional dissipation parameter]. Previous studies have mentioned the importance of appropriate damping to a dynamic model (e.g., Hall and Sardeshmukh 1998; Zhang and Held 1999). A total of N normal modes are generated (N is the total grid points in the selected two-dimensional gridded field) by solving an eigenvalue–eigenvector problem. Then, we make use of all the resulting normal modes as base functions to compute optimal modes over the optimization time τ. Following previous studies (e.g., Borges and Hartmann 1992; Chang and Mak 1995; Mitas and Robinson 2005; Mak 2011a,b; Zhao et al. 2018), the intensity of a disturbance (measured in terms of energy norm) at $t = \tau$ is defined as

$$A(\tau) = \boldsymbol{\psi}^H \mathbf{D} \boldsymbol{\psi}, \tag{1}$$

where $\boldsymbol{\psi}$ is streamfunction perturbation, $\boldsymbol{\psi}^H$ is the Hermitian of $\boldsymbol{\psi}$, and $\mathbf{D}$ is a unit matrix. Here we adopt the norm used in such analyses. Other forms of norms have also been used before. For example, in studies of SST variability, the norm has been defined as domain-mean square amplitude of SST anomalies (e.g., Newman et al. 2011; Vimont et al. 2014). After solving an eigenvalue–eigenvector problem again, a total of N optimal modes is obtained for each optimization time τ. For a specified optimization time, the optimal mode with the largest amplification factor (i.e., the ratio between the intensity of a disturbance at $t = \tau$ and $t = 0$) is denoted as the first optimal mode. The remaining optimal modes are ordered in the sequence of the magnitude of amplification factor and are denoted as the second optimal mode, third optimal mode, and so on. The full derivation of the NIA for the barotropic model can be found in Zhao et al. (2018).

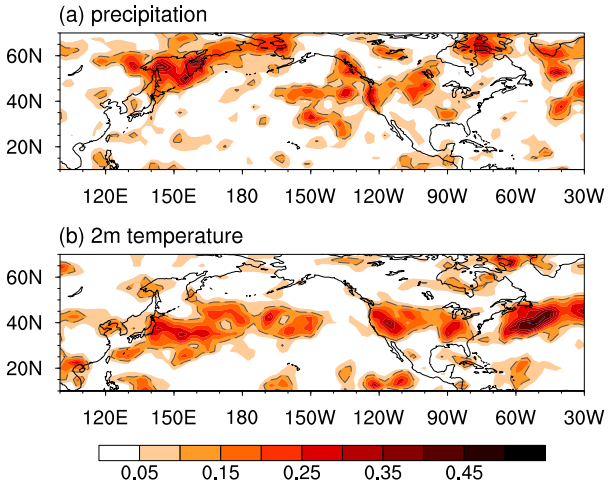

FIG. 3. (a) The coefficient of determination R^2 for the regression of precipitation onto EKE. (b) As in (a), but for the regression of 2-m temperature onto EKE. Contours are significant at the 0.05 level.

d. *Nonmodal instability analysis using a two-level QG model*

We derive the two-level QG potential vorticity (QGPV) equation in spherical coordinates starting from the QG vorticity equation [Eq. (6.71) of Mak (2011a)] and QG thermodynamic equation [Eq. (6.72) of Mak (2011a)]. By substituting geostrophic balance and continuity equation into the QG vorticity equation, applying the QG vorticity equation for the upper and lower levels (i.e., 300 and 700 hPa), and making use of vertical boundary condition, the QG vorticity equation at two levels could be expressed as

$$\frac{\partial \zeta_1}{\partial t} + f^{-1}J(Z_1, \zeta_1 + f) = f\frac{\omega_2}{\delta p} - \kappa\zeta_1,$$

$$\frac{\partial \zeta_3}{\partial t} + f^{-1}J(Z_3, \zeta_3 + f) = -f\frac{\omega_2}{\delta p} - \kappa\zeta_3. \qquad (2)$$

In (2), subscripts 1, 2, and 3 refer to the upper, middle (500 hPa), and lower levels, respectively; $J(A, B) = (\partial A/\partial x)(\partial B/\partial y) - (\partial A/\partial y)(\partial B/\partial x)$ is the Jacobian ($\partial x = r\cos\varphi\,\partial\lambda$ and $\partial y = r\partial\varphi$; r is Earth's radius; and φ and λ are the latitude and longitude, respectively). Also, ζ and Z are the geostrophic vorticity and geopotential, respectively, with a relation of $\zeta = f^{-1}\mathscr{L}\{Z\}$ ($\mathscr{L}\{\cdots\}$ is the Laplacian operator); f, δp, κ, and ω are the Coriolis frequency, thickness of the layer, frictional dissipation parameter, and vertical velocity, respectively. Then, by applying the QG thermodynamic equation for the middle level and assuming $Z_2 = (Z_1 + Z_3)/2$, the QG thermodynamic equation at the middle level is

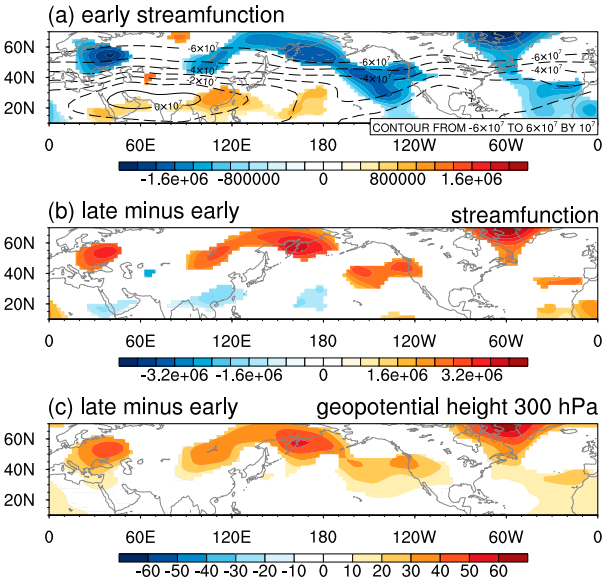

FIG. 4. (a) The summer-mean 250-hPa streamfunction (contours; $m^2\,s^{-1}$) and its anomaly (shading; $m^2\,s^{-1}$) averaged for the early period. (b) The difference in summer-mean 250-hPa streamfunction anomaly ($m^2\,s^{-1}$) between the late and early periods (the former minus the latter). (c) As in (b), but for summer-mean 300-hPa geopotential height (m). Only significance at the 0.05 level is shown.

$$\frac{\partial}{\partial t}\left[\frac{f(Z_3 - Z_1)}{(\delta p)^2 S_2}\right] + \frac{1}{(\delta p)^2 S_2}J(Z_1, Z_3) = -f\frac{\omega_2}{\delta p}, \qquad (3)$$

where S is the static stability parameter. By combining (2) and (3), we get the QGPV equation in spherical coordinates for the upper and lower levels:

$$\frac{\partial}{\partial t}\left[\zeta_1 + \frac{f(Z_3 - Z_1)}{(\delta p)^2 S_2}\right] + f^{-1}J(Z_1, \zeta_1 + f) + \frac{1}{(\delta p)^2 S_2}J(Z_1, Z_3) = -\kappa\zeta_1,$$

$$\frac{\partial}{\partial t}\left[\zeta_3 + \frac{f(Z_1 - Z_3)}{(\delta p)^2 S_2}\right] + f^{-1}J(Z_3, \zeta_3 + f) + \frac{1}{(\delta p)^2 S_2}J(Z_3, Z_1) = -\kappa\zeta_3. \qquad (4)$$

We linearize the above equation and assume solutions for the upper and lower perturbation (note that ζ could be replaced by Z through the Laplacian operator shown above):

$$Z_j'(\lambda, \varphi, t) = \phi_j(\lambda, \varphi)e^{I\sigma t}, \quad j = 1, 3, \qquad (5)$$

where $\phi(\lambda, \varphi)$ is the perturbation amplitude, I is the imaginary unit, and σ is the frequency of oscillation.

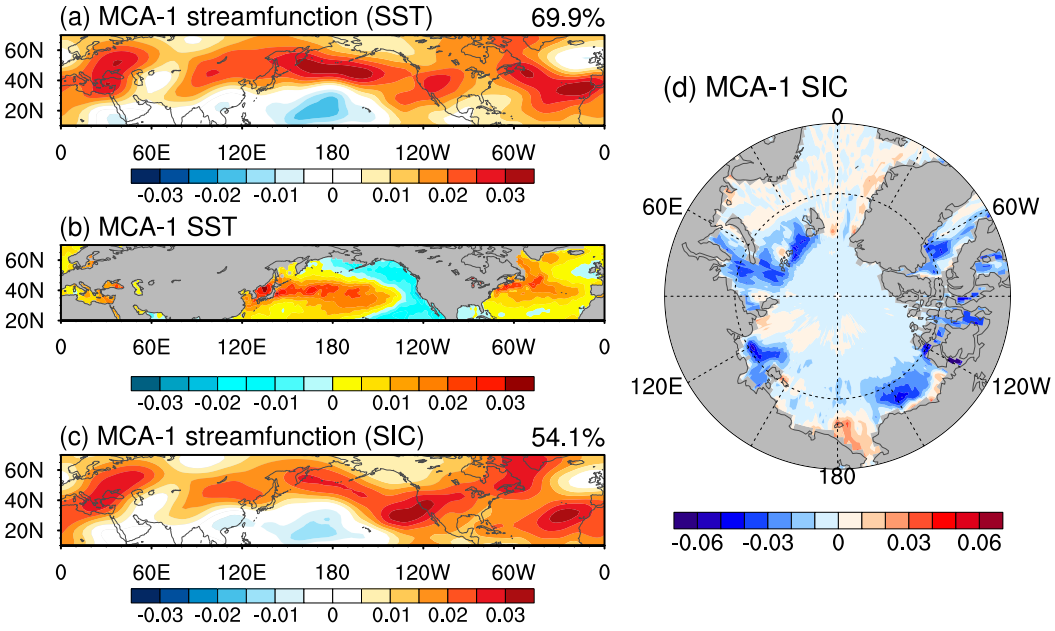

FIG. 5. (a) Singular vectors for the summer-mean 250-hPa streamfunction corresponding to the first MCA mode resulting from the MCA between the undetrended streamfunction and SST. (b) As in (a), but for SST. (c) As in (a), but for the first MCA mode resulting from the MCA between the undetrended streamfunction and SIC. (d) As in (c), but for the SIC. The number shown in the top-right corner of (a) and (c) is the percentage of the total squared covariance for the coupled mode.

After substituting solutions into the linearized equation, discretizing the equation, and applying cyclical boundary conditions, we obtain the matrix equation:

$$\sigma \mathbf{L}\begin{pmatrix}\mathbf{\Phi}_1\\ \mathbf{\Phi}_3\end{pmatrix} = \mathbf{R}\begin{pmatrix}\mathbf{\Phi}_1\\ \mathbf{\Phi}_3\end{pmatrix}, \tag{6}$$

where $\mathbf{L}$ and $\mathbf{R}$ are matrices ($2N \times 2N$) and $\mathbf{\Phi}_1$ and $\mathbf{\Phi}_3$ are vectors ($N \times 1$). The intensity of a disturbance at $t = \tau$ is defined as $A(\tau) = \mathbf{Z}^H\mathbf{D}\mathbf{Z}$, where $\mathbf{Z}$ is geopotential perturbation. The following procedures calculating normal and optimal modes are almost the same as those for the barotropic model [see Zhao et al. (2018) for details]. The only difference is that the total grid points are larger ($2N$) since we combine the upper and lower levels together. Finally, a total of $2N$ optimal modes is obtained for each optimization time τ.

3. Results

a. *Observed changes in the northern midlatitude summer climate*

Figure 1a shows the summer-mean precipitation anomaly averaged over 30°–50°N during the early (1979–94) and late (2000–15) periods (similar results are obtained if averaged over 30°–60°N). In the Pacific–North America–North Atlantic sector, the precipitation anomaly is generally positive (negative) for the early (late) period, indicating a phase shift of summer precipitation in midlatitudes (Figs. 1a and 2a,b). The anomaly is significant at the 0.05 level over East Asia and North Pacific (such significance could be more easily seen in Fig. 2). It is also noted that the outstanding negative (positive) precipitation anomaly around 150°E and 80°W for early (late) period is probably due to the change in the frequency or intensity of tropical cyclones that made landfall over Japan and eastern United States (e.g., Emanuel 2005; Webster et al. 2005). Compared to the precipitation anomaly, the difference in 2-m temperature anomaly between the early and late periods is more significant (Figs. 1b and 2c,d). We additionally calculate summer heat wave days (i.e., extreme hot days) over the western North America and East Asia, respectively (see section 2 for details). Results show that there exists a significant upward trend of heat wave days for both two regions, while the trend for East Asia (significant at the 0.01 level) is more significant than that for North America (significant at the 0.1 level) (Figs. 1c,d). The results presented above suggest that the midlatitude summer in the Pacific–North America–North Atlantic sector is generally becoming dryer and warmer during the past 40 years.

Synoptic variability is typically associated with fast-propagating Rossby waves with zonal wavenumber

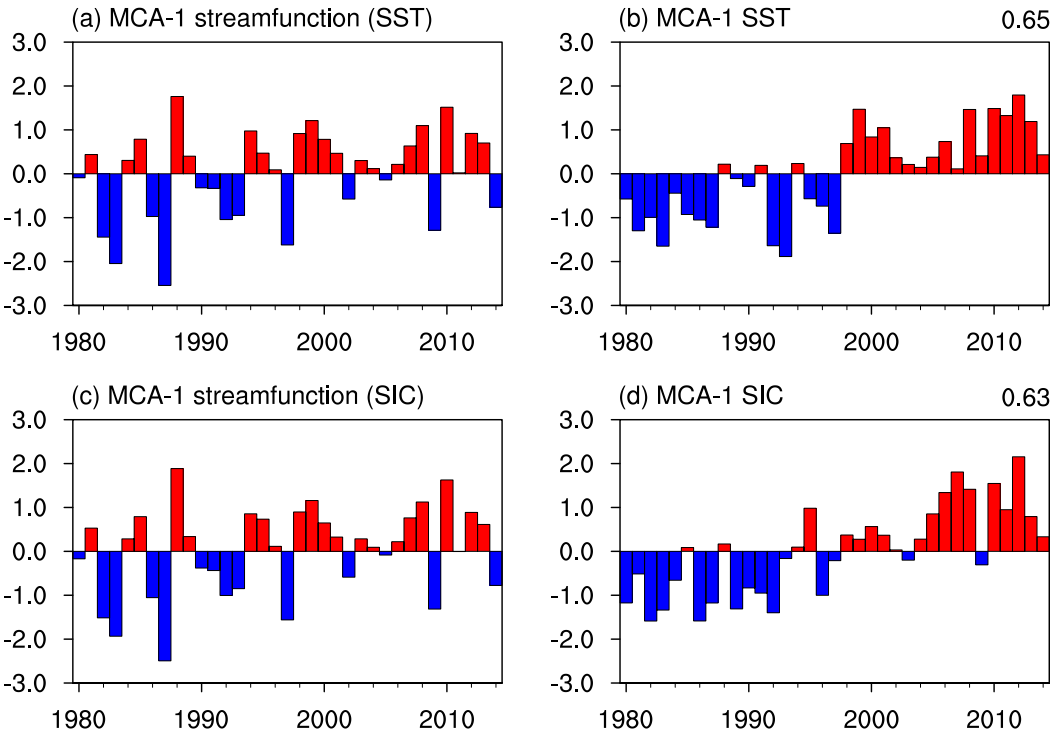

FIG. 6. (a) Expansion coefficients for the summer-mean 250-hPa streamfunction corresponding to the first MCA mode resulting from the MCA between the undetrended streamfunction and SST. (b) As in (a), but for the SST. (c) As in (a), but for the first MCA mode resulting from the MCA between the undetrended streamfunction and SIC. (d) As in (c), but for the SIC. The number shown in the top-right corner of (b) and (d) is the correlation coefficient of the expansion coefficients of the coupled fields.

greater than 6 (e.g., Coumou et al. 2015). These synoptic-scale disturbances form the midlatitude storm track and their passages often bring precipitation and cool weather to subtropical and midlatitude regions in summer. As shown in Lehmann and Coumou (2015) and Chang et al. (2016), low synoptic variability and EKE result in less frequent cool maritime air masses and decrease in cloud cover, favoring persistent heat waves and drought. Here we quantify the synoptic variability by computing the root-mean-square (RMS) of 2.5–6-day Butterworth bandpass-filtered 250-hPa streamfunction during summer (Russell 2006). Figure 1e shows the composite anomaly of the RMS averaged over 30°–50°N during the early and late periods. The RMS anomaly is generally positive (negative) over two ocean basins (significant at the 0.05 level over the North Pacific; such significance could be more easily seen in Fig. 2) for the early (late) period, except for some regions over North America (Figs. 1e and 2e,f), where changes in tropical cyclone activities might be important (e.g., Emanuel 2005; Webster et al. 2005). When evaluated in terms of EKE (the summer-mean EKE is based on 2.5–6-day bandpass-filtered daily winds) (e.g., McCrary et al. 2014; Coumou et al. 2015; Li et al. 2015), the synoptic variability also exhibits a phase shift, especially over the two ocean basins (Figs. 1f and 2g,h). The declining summer EKE is generally consistent with that reported in Coumou et al. (2015).

To further examine how much precipitation or temperature variability is explained by local EKE change, we perform a linear regression analysis by regressing annual-mean summer precipitation and 2-m temperature onto annual-mean summer EKE. The coefficient of determination R^2 is plotted in Fig. 3 and an F test is applied to examine the significance of R^2 (e.g., An et al. 2014; Harding and Snyder 2015; Infanti and Kirtman 2016). The results imply that around 20%–30% (significant at the 0.05 level) of the precipitation variability can be accounted for by EKE over the high latitudes, eastern North Pacific, and part of North America (Fig. 3a). For 2-m temperature, the coefficient of determination above 0.2 is generally over 30°–50°N. We thus infer that the observed trend in midlatitude synoptic variability can at least partly explain the trends in precipitation and temperature. Also note that global warming may also be a driver of heat extremes (e.g., Coumou and Rahmstorf 2012). A similar linear regression analysis suggests that the connection

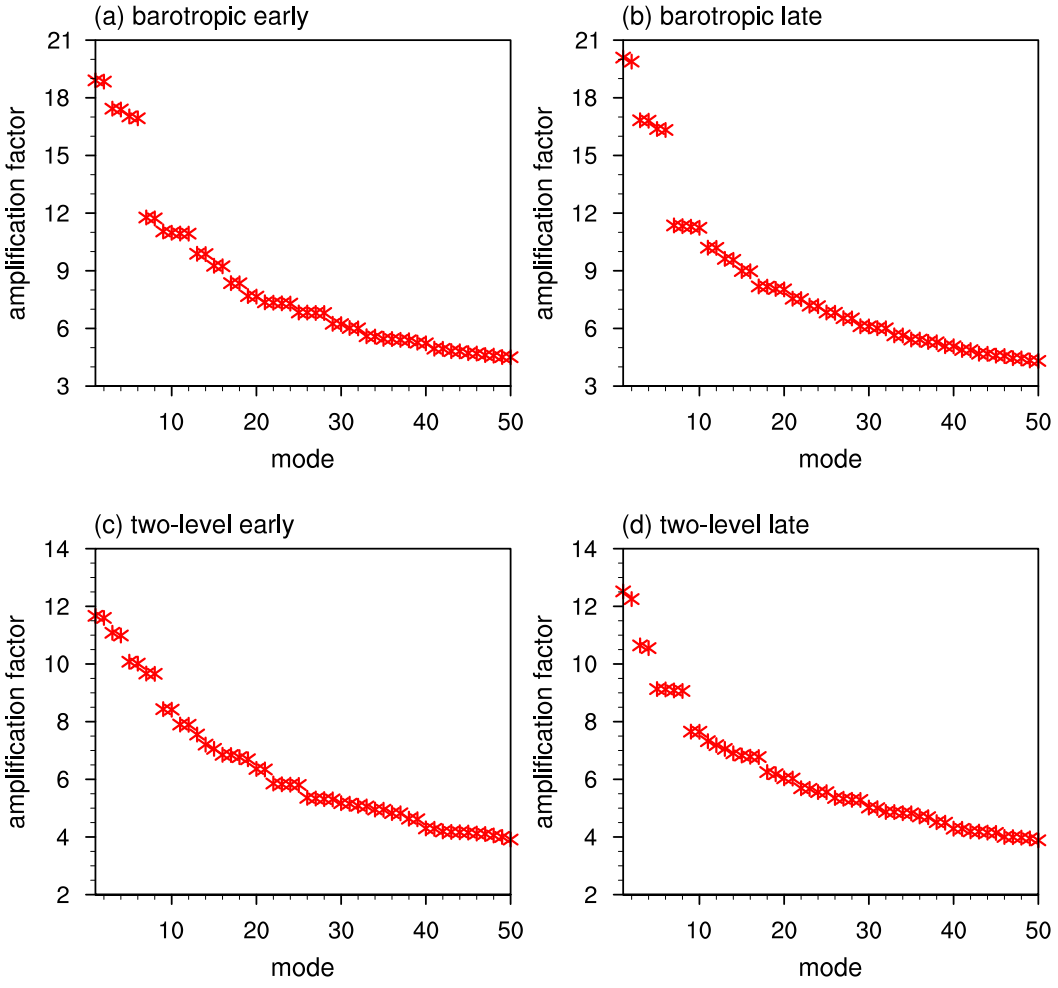

FIG. 7. (a) Amplification factor for the first 50 optimal modes for the optimization time $\tau = 1.5$ days during the early period in the barotropic model. (b) As in (a), but for the late period. (c),(d) As in (a) and (b), but for the two-level QG model.

between the precipitation and global warming trend is quite weak, while such a trend could explain more than 30% of the variance of temperature variability over East Asia and part of the two ocean basins (figure not shown).

The change in the background flow during the two periods is also significant. Figure 4a displays the summer-mean 250-hPa streamfunction and its anomaly for the early period. The summer-mean upper-tropospheric streamfunction typically decreases from low to high latitudes (see the contour). The anomaly field (shading; significant at the 0.05 level) is characterized by negative streamfunction anomalies over eastern Europe, the Bering Sea, and the northeastern Pacific and Atlantic and positive anomalies over the subtropics of the Eastern Hemisphere. Since negative (positive) streamfunction anomaly is usually associated with cyclonic (anticyclonic) circulation anomalies, it can be inferred that there is a stronger westerly jet over the midlatitude North Pacific during the early period. It is known that such a westerly jet can act as a waveguide (e.g., Hoskins and Ambrizzi 1993; Nishii and Nakamura 2004). The difference in the streamfunction anomaly between the late and early period indicates that the late period anomaly corresponds to almost the exact opposite phase of the early-period one (Fig. 4b). A weakened westerly jet may be inferred from the streamfunction anomaly during the late period and this is consistent with the findings in Coumou et al. (2015). The background flow difference for the two periods in terms of geopotential height at 300 (Fig. 4c) and 700 hPa (figure not shown) is similar to that of streamfunction.

Previous studies have shown that variations in mid-latitude summer circulations are likely related to Arctic warming and decadal-scale SST variability (e.g., Seager et al. 2010; Mills and Walsh 2013; Cohen et al. 2014;

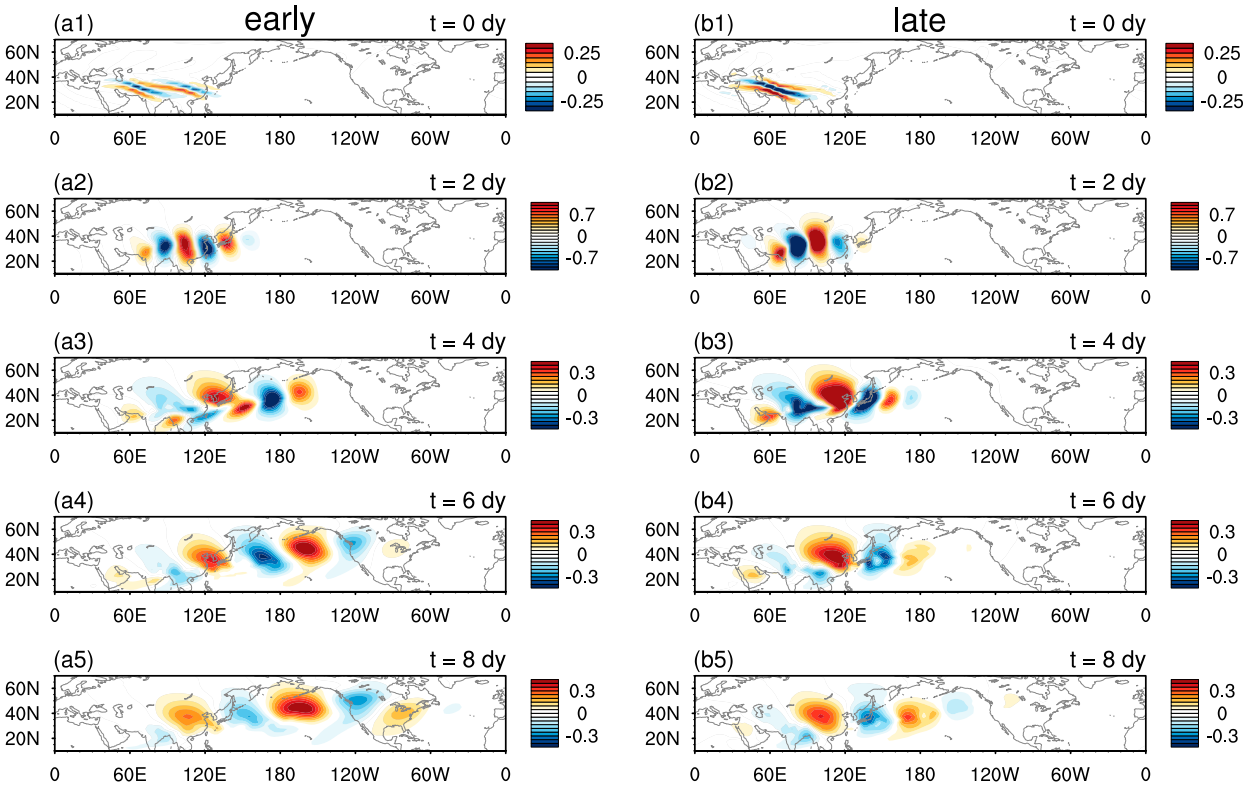

FIG. 8. (a) The time evolution [for (top to bottom) $t = 0, 2, 4, 6$, and 8 days] of the first optimal mode for the optimization time $\tau = 1.5$ days during the early period in the barotropic model. (b) As in (a), but for the late period.

Zhao et al. 2017b; Coumou et al. 2018). During the past 40 years, there existed a significant downward (upward) trend within the PDO (AMO) index, which may reflect the phase transition of PDO (AMO) that occurred around 1997–98 (Dai 2013; Stolpe et al. 2017). Following these studies, we first conduct an MCA for the summer-mean *undetrended* streamfunction and *undetrended* SST and SIC during the period of 1979–2015 to reveal their covarying patterns (see section 2 for details). Figures 5a and 5b display the first MCA mode (MCA-1; which accounts for 69.9% of the total squared covariance) of the summer-mean 250-hPa streamfunction and SST. The streamfunction anomaly of MCA-1 tends to occur in association with a SST anomaly pattern that is a combination of the negative PDO (in the Pacific sector) and positive AMO (in the Atlantic sector). The correlation coefficient of the expansion coefficients (time series) corresponding to the MCA-1 of the streamfunction and SST is 0.65, indicating a moderate correlation between the coupled fields (Figs. 6a,b). The correlation coefficient between the expansion coefficients of SST and AMO (PDO) index is 0.64 (−0.92), much higher than that between the expansion coefficients of streamfunction and these indices. In addition, the MCA-1 of the summer-mean undetrended 250-hPa streamfunction and undetrended SIC shows that changes in midlatitude summer-mean circulation are also connected to changes in SIC, with a correlation coefficient around 0.63 (Figs. 5c,d and 6c,d). The correlation between SIC and AMO/PDO index is generally weaker. When we conduct the MCA for the *detrended* fields, very similar spatial structures (figure not shown) and a higher correlation (around 0.80) between streamfunction and SIC could be obtained. The results of the MCA show that these fields might relate to each other and provide an observational basis for formulating physical hypotheses regarding the potential coupling between the two fields.

b. *Changes in the excitation of synoptic variability viewed from nonmodal instability perspective*

The previous section represents the change in midlatitude summer synoptic variability and associated weather extremes such as heat waves and droughts. In this section, we further investigate the dynamic origin, precursor disturbance, and wave propagation responsible for the observed changes in synoptic variability. Here we hypothesize that the changing synoptic disturbance activities in the two periods are the result of changing optimal disturbance growth in a changing

summer background flow. We will test this hypothesis by identifying the optimal disturbances through the NIA applied to the summer-mean flow in the early and late periods.

We first carry out the NIA in a barotropic model [see section 2 and Zhao et al. (2018) for details] and consider summer-mean 250-hPa streamfunction during the early and late periods as background flows. Previous studies suggested that a realistic value for the dissipation time scale κ^{-1} in the upper troposphere is about 5 days (e.g., Borges and Sardeshmukh 1995; Mitas and Robinson 2005). We set κ^{-1} to be 5 days in the barotropic model. The top three most unstable normal modes are evaluated for early and late periods, respectively. The growth rates in terms of *e*-folding time scales for these most unstable modes are around 4.1 days. They all show a circumglobal wave train pattern yet bear little similarity to the structure of synoptic-scale disturbances over the Northern Hemisphere (figure not shown). It is also found that the spatial scale of these waves in early period is larger than those in the late period. To get rapidly amplifying disturbance within a basic flow, the optimal mode will be subsequently studied. Given the typical 2.5–6-day lifespan of synoptic-scale disturbances, here we assess the optimal modes of the summer-mean flow for an optimization time τ of 1–2 days (i.e., close to one-fourth of the total lifespan). Substantial and consistent differences are found between the two periods for the optimization time considered above. In the following discussion, for brevity, we will show the results for τ = 1.5 days.

Figure 7a shows amplification factors for the first 50 optimal modes for the optimization time τ = 1.5 days during the early period. The amplification factors decrease from the first to the fiftieth optimal mode. Figure 8a shows the time evolution map (t = 0, 2, 4, 6, and 8 days) of the first optimal mode during the early period. The initial disturbance (i.e., at t = 0 days) of the first optimal mode first appears over central and East Asia [between 20° and 40°N; Fig. 8a(1)] and it intensifies the most by t = 1.5 days. At around t = 8 days, the wave train crosses North America and reaches the Atlantic [Fig. 8a(5)]. For the late period, however, the initial disturbance appears over central Asia [Fig. 8b(1)], and the wave train takes much longer time to reach North America or even the Atlantic [Fig. 8b(5)]. Such differences between the two periods are likely due to a weaker westerly jet (which acts as a waveguide) over the midlatitude North Pacific during the late period.

Earlier studies have shown that variance of transients from multiple short-term integrations of a linear storm track model could be used to estimate activities of storm tracks (synoptic-scale variability) (e.g., Branstator 1995; Gritsun et al. 2008). Here we resort to a similar approach by considering the evolution in each day (from t = 0 to t = 8 days; 9 days in total) of each optimal disturbance as an individual case and compute the variance (RMS) of the top 5, 10, 20, and 50 optimal disturbances (normalization of the amplitude of each mode has been applied), respectively, to provide a more objective assessment of the general synoptic-scale variability. Figure 9a shows the difference in the RMS of the first five optimal modes (i.e., total of 45 cases) between the late and early period (the former minus the latter). Synoptic variability quantified in this way shows a general suppression of wave activities during the late period in northern midlatitudes, especially over the North Pacific. Similar results are shown for the first 10, 20, and 50 optimal modes (Figs. 9b–d). However, the spatial scale of these optimal modes is greater than that of synoptic-scale disturbances. To better represent the synoptic variability, we adopt a two-level QG model to further investigate the changing optimal disturbance excitation during the two periods.

In the two-level QG model, the basic state is the summer-mean 300- and 700-hPa geopotential (i.e., $\overline{Z_1}$ and $\overline{Z_3}$), which is the product of geopotential height and gravitational acceleration. The static stability parameter at the middle level S_2 is considered as a constant with the typical value of $3.1 \times 10^{-6}\,\mathrm{m^2\,Pa^{-2}\,s^{-2}}$ for 500 hPa in midlatitude summer. Similar to that in the

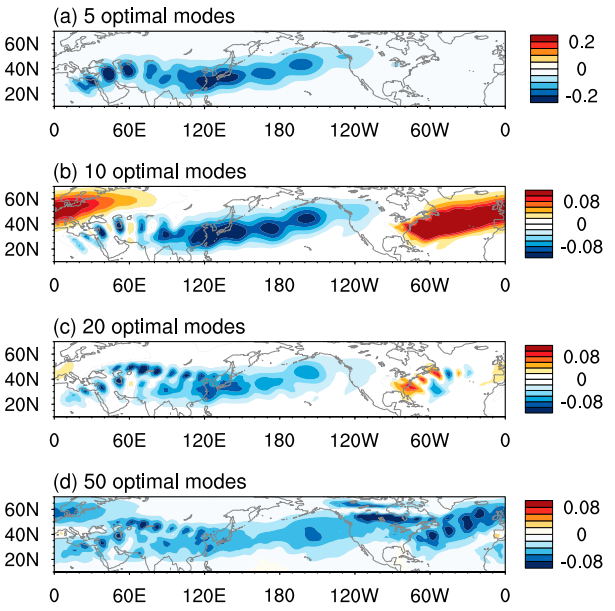

FIG. 9. (a) The difference in the RMS of the first 5 optimal modes between the late and early period (the former minus the latter) in the barotropic model. (b)–(d) As in (a), but for the first 10, 20, and 50 optimal modes.

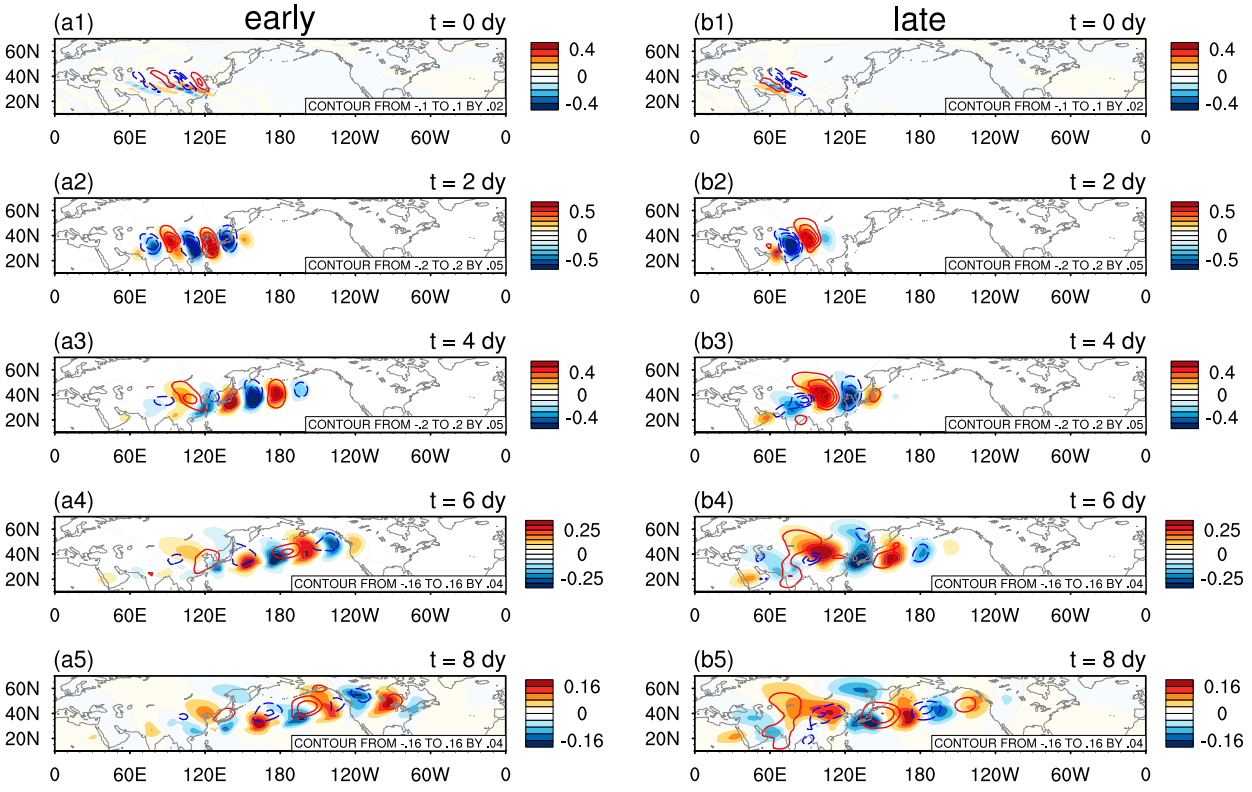

FIG. 10. (a) As in Fig. 8a, but for the first optimal mode for the optimization time $\tau = 1.5$ days at 300 hPa (shading) and 700 hPa (contours) during the early period in the two-level QG model. (b) As in (a), but for the late period.

barotropic model, we set dissipation time scale κ^{-1} at 300 hPa to be 5 days. For 700 hPa, considering the topography effect and land–ocean difference, we set the dissipation time scale to be 3 days over the ocean and 1.4–3 days over the land [the higher (lower) the summer-mean surface pressure is, the larger (smaller) the dissipation time scale is]. For example, the value for the Tibetan Plateau (with very low surface pressure) is around 1.4 days, indicating a very strong damping effect there. The *e*-folding time scales of the topmost unstable normal modes in the two-level model are around 1.5 days. The spatial structures of the normal modes for the early and late periods are similar, with a large-scale dipole structure over the Eastern Hemisphere at upper levels and small-scale disturbances over central Asia at lower levels (figure not shown). Following the NIA in the barotropic model, we still compare the optimal modes of the early and late periods when $\tau = 1.5$ days (similar results can be found when τ ranges from 1 to 2 days).

Figure 10a shows the time evolution map of the first optimal mode at 300 (shading) and 700 (contours) hPa during the early period. When the wave train and associated energy propagate downstream, troughs/ridges leading the wave train also move eastward and some falling behind just dissipate. After $t = 4$ days, the optimal disturbances at the two levels become more barotropic, even attaining a slight eastward tilt, which is largely consistent with the life cycle of baroclinic eddies. The fast-propagating wave train extends through North America to the Atlantic at around $t = 8$ days [Fig. 10a(5)]. The optimal growth for the late period is mainly confined in the North Pacific (Fig. 10b), which is similar to the results in the barotropic model (Fig. 8b). Compared to the first optimal mode in the barotropic model, the one obtained in the two-level QG mode has a smaller spatial scale, closer to the synoptic-scale waves. Figure 11 displays the difference in the RMS of the first 5, 10, 20, and 50 optimal modes (their spatial scales are closer to synoptic scale), respectively, between the late and early period (the former minus the latter). A suppression of wave activities is shown over the North Pacific and North Atlantic (albeit with some inconsistency in Fig. 11a), generally consistent with the finding in the observation. These results highlight the importance of the changing summer background flow in contributing to the observed changes in synoptic variability and suggest that nonmodal growth in a changing background flow is at least partly responsible for the observed changes.

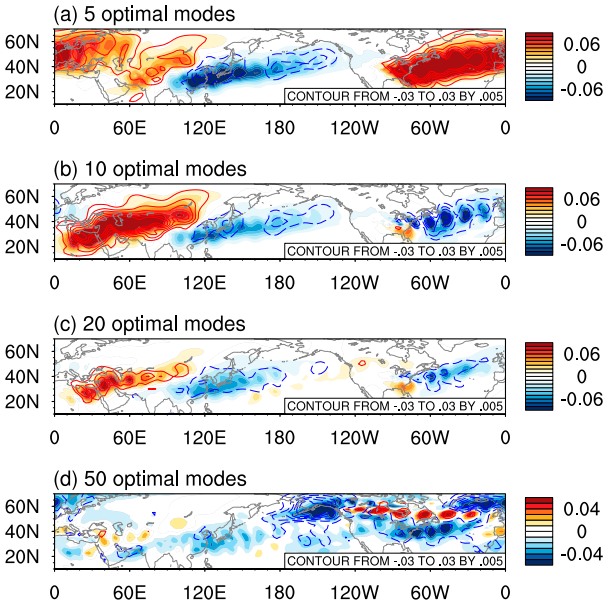

FIG. 11. (a) As in Fig. 9a, but for the difference in the RMS of the first 5 optimal modes at 300 hPa (shading) and 700 hPa (contours) in the two-level QG model. (b)–(d) As in (a), but for the first 10, 20, and 50 optimal modes.

4. Summary and concluding remarks

This study investigates the dynamical processes potentially responsible for long-term changes in the boreal summer synoptic variability in the northern midlatitudes. Over the past 40 years, the northern midlatitude summer is becoming dryer and warmer in the Pacific–North America–North Atlantic sector, partly driven by the declining synoptic variability, especially over the North Pacific and North Atlantic. The corresponding changes in the summer background flow are characterized by weakened westerly jets in the northern midlatitudes. An MCA applied to the summer-mean flow and North Pacific/North Atlantic SST and Arctic SIC reveals the potential connections between the observed mean-flow change and phase transition of the PDO/AMO as well as the changing SIC in recent decades.

An NIA of the summer-mean flow for the early (1979–94) and late (2000–15) periods suggests that the decline of synoptic variability in the late period can at least partially be explained in terms of the changes in the properties of optimal disturbances that intensify the most over a 1–2-day interval. This result is confirmed by both a barotropic and a two-level QG model, with the two-level model successfully simulating the typical spatial scales of midlatitude synoptic waves. Specifically, in the two-level model, the precursor disturbance of the leading mode appears over central Asia and East Asia in the early studying period, whereas that in the late period is mainly confined in the North Pacific. The model synoptic variability associated with the top (up to 50) optimal disturbances also indicates a suppression of wave activities in northern midlatitudes during the late period. These results suggest the importance of changing summer background flow and the associated nonmodal instability properties in helping understand long-term changes in summer synoptic variability.

One caveat of the current study is that the results of nonmodal instability analysis could depend on the exact form of the norm used to measure the strength of the disturbance. We are currently investigating such sensitivities. Future analyses may also include an examination of the excitation of synoptic variability in a predicted background flow associated with ongoing global climate change. Finally, changes in latent heating within synoptic-scale disturbances associated with global warming and increased atmospheric moisture content could play an important role in determining the overall trend in local activity of such disturbances (e.g., Emanuel et al. 1987; Held 1993). The potential role of latent heating change is worth exploring in the future.

Acknowledgments. We thank the two anonymous reviewers for their insightful comments. This study is supported by the National Science Foundation Climate and Large-Scale Dynamics (CLD) program through Grants AGS-1354402 and AGS-1445956 and by the National Oceanic and Atmospheric Administration through Award NA16NWS4680013.

REFERENCES

Adler, R. F., and Coauthors, 2003: The version-2 Global Precipitation Climatology Project (GPCP) monthly precipitation analysis (1979–present). *J. Hydrometeor.*, **4**, 1147–1167, https://doi.org/10.1175/1525-7541(2003)004<1147:TVGPCP>2.0.CO;2.

An, W., X. Liu, S. W. Leavitt, G. Xu, X. Zeng, W. Wang, D. Qin, and J. Ren, 2014: Relative humidity history on the Batang–Litang Plateau of western China since 1755 reconstructed from tree-ring δ18O and δD data. *Climate Dyn.*, **42**, 2639–2654, https://doi.org/10.1007/s00382-013-1937-z.

Borges, M. D., and D. L. Hartmann, 1992: Barotropic instability and optimal perturbations of observed nonzonal flows. *J. Atmos. Sci.*, **49**, 335–354, https://doi.org/10.1175/1520-0469(1992)049<0335:BIAOPO>2.0.CO;2.

——, and P. D. Sardeshmukh, 1995: Barotropic Rossby wave dynamics of zonally varying upper-level flows during northern winter. *J. Atmos. Sci.*, **52**, 3779–3796, https://doi.org/10.1175/1520-0469(1995)052<3779:BRWDOZ>2.0.CO;2.

Branstator, G., 1995: Organization of storm track anomalies by recurring low-frequency circulation anomalies. *J. Atmos. Sci.*, **52**, 207–226, https://doi.org/10.1175/1520-0469(1995)052<0207:OOSTAB>2.0.CO;2.

——, 2002: Circumglobal teleconnections, the jet stream waveguide, and the North Atlantic Oscillation. *J. Climate*, **15**,

1893–1910, https://doi.org/10.1175/1520-0442(2002)015<1893:CTTJSW>2.0.CO;2.

Bretherton, C. S., C. S. Smith, and J. M. Wallace, 1992: An intercomparison of methods for finding coupled patterns in climate data. *J. Climate*, **5**, 541–560, https://doi.org/10.1175/1520-0442(1992)005<0541:AIOMFF>2.0.CO;2.

Brewer, M. C., and C. F. Mass, 2016a: Projected changes in western U.S. large-scale summer synoptic circulations and variability in CMIP5 models. *J. Climate*, **29**, 5965–5978, https://doi.org/10.1175/JCLI-D-15-0598.1.

——, and ——, 2016b: Projected changes in heat extremes and associated synoptic- and mesoscale conditions over the Northwest United States. *J. Climate*, **29**, 6383–6400, https://doi.org/10.1175/JCLI-D-15-0641.1.

Chang, E. K. M., C. G. Ma, C. Zheng, and A. M. W. Yau, 2016: Observed and projected decrease in Northern Hemisphere extratropical cyclone activity in summer and its impacts on maximum temperature. *Geophys. Res. Lett.*, **43**, 2200–2208, https://doi.org/10.1002/2016GL068172.

Chang, J.-C., and M. Mak, 1995: Nonmodal barotropic dynamics of the intraseasonal disturbances. *J. Atmos. Sci.*, **52**, 896–914, https://doi.org/10.1175/1520-0469(1995)052<0896:NBDOTI>2.0.CO;2.

Cohen, J., and Coauthors, 2014: Recent Arctic amplification and extreme mid-latitude weather. *Nat. Geosci.*, **7**, 627–637, https://doi.org/10.1038/ngeo2234.

Coumou, D., and S. Rahmstorf, 2012: A decade of weather extremes. *Nat. Climate Change*, **2**, 491–496, https://doi.org/10.1038/nclimate1452.

——, J. Lehmann, and J. Beckmann, 2015: The weakening summer circulation in the Northern Hemisphere mid-latitudes. *Science*, **348**, 324–327, https://doi.org/10.1126/science.1261768.

——, G. Di Capua, S. Vavrus, L. Wang, and S. Wang, 2018: The influence of Arctic amplification on mid-latitude summer circulation. *Nat. Commun.*, **9**, 2959, https://doi.org/10.1038/s41467-018-05256-8.

Czaja, A., and C. Frankignoul, 2002: Observed impact of Atlantic SST anomalies on the North Atlantic Oscillation. *J. Climate*, **15**, 606–623, https://doi.org/10.1175/1520-0442(2002)015<0606:OIOASA>2.0.CO;2.

Dai, A., 2013: The influence of the inter-decadal Pacific oscillation on U.S. precipitation during 1923–2010. *Climate Dyn.*, **41**, 633–646, https://doi.org/10.1007/s00382-012-1446-5.

Dee, D. P., and Coauthors, 2011: The ERA-Interim reanalysis: Configuration and performance of the data assimilation system. *Quart. J. Roy. Meteor. Soc.*, **137**, 553–597, https://doi.org/10.1002/qj.828.

Ding, Q. H., and B. Wang, 2005: Circumglobal teleconnection in the Northern Hemisphere summer. *J. Climate*, **18**, 3483–3505, https://doi.org/10.1175/JCLI3473.1.

Donat, M., A. Lowry, L. Alexander, P. O'Gorman, and N. Maher, 2016: More extreme precipitation in the world's dry and wet regions. *Nat. Climate Change*, **6**, 508–513, https://doi.org/10.1038/nclimate2941.

Emanuel, K., 2005: Increasing destructiveness of tropical cyclones over the past 30 years. *Nature*, **436**, 686–688, https://doi.org/10.1038/nature03906.

——, M. Fantini, and A. J. Thorpe, 1987: Baroclinic instability in an environment of small stability to slantwise moist convection. Part I: Two-dimensional models. *J. Atmos. Sci.*, **44**, 1559–1573, https://doi.org/10.1175/1520-0469(1987)044<1559:BIIAEO>2.0.CO;2.

Farrell, B. F., 1988: Optimal excitation of neutral Rossby waves. *J. Atmos. Sci.*, **45**, 163–172, https://doi.org/10.1175/1520-0469(1988)045<0163:OEONRW>2.0.CO;2.

——, 1989: Optimal excitation of baroclinic waves. *J. Atmos. Sci.*, **46**, 1193–1206, https://doi.org/10.1175/1520-0469(1989)046<1193:OEOBW>2.0.CO;2.

Fischer, E. M., and R. Knutti, 2015: Anthropogenic contribution to global occurrence of heavy-precipitation and high-temperature extremes. *Nat. Climate Change*, **5**, 560–564, https://doi.org/10.1038/nclimate2617.

Gritsun, A., G. Branstator, and A. Majda, 2008: Climate response of linear and quadratic functionals using the fluctuation–dissipation theorem. *J. Atmos. Sci.*, **65**, 2824–2841, https://doi.org/10.1175/2007JAS2496.1.

Groisman, P. Ya., and Coauthors, 1999: Changes in the probability of heavy precipitation: Important indicators of climatic change. *Climatic Change*, **42**, 243–283, https://doi.org/10.1023/A:1005432803188.

——, R. W. Knight, D. Easterling, T. Karl, G. Hegerl, and V. Razuvaev, 2005: Trends in intense precipitation in the climate record. *J. Climate*, **18**, 1326–1350, https://doi.org/10.1175/JCLI3339.1.

Hakim, G. J., 2000: Role of nonmodal growth and nonlinearity in cyclogenesis initial-value problems. *J. Atmos. Sci.*, **57**, 2951–2967, https://doi.org/10.1175/1520-0469(2000)057<2951:RONGAN>2.0.CO;2.

Hall, N. M., and P. D. Sardeshmukh, 1998: Is the time-mean Northern Hemisphere flow baroclinically unstable? *J. Atmos. Sci.*, **55**, 41–56, https://doi.org/10.1175/1520-0469(1998)055<0041:ITTMNH>2.0.CO;2.

Harding, K. J., and P. K. Snyder, 2015: The relationship between the Pacific–North American teleconnection pattern, the Great Plains low-level jet, and North Central U.S. heavy rainfall events. *J. Climate*, **28**, 6729–6742, https://doi.org/10.1175/JCLI-D-14-00657.1.

Hartmann, D. L., 2016: Matrix methods for analysis of structure in data sets. Matrix methods: EOF, SVD, ETC., University of Washington Department of Atmospheric Sciences objective analysis course notes, 103 pp, https://atmos.washington.edu/~dennis/552_Notes_4.pdf.

Held, I. M., 1993: Large-scale dynamics and global warming. *Bull. Amer. Meteor. Soc.*, **74**, 228–242, https://doi.org/10.1175/1520-0477(1993)074<0228:LSDAGW>2.0.CO;2.

——, and B. J. Soden, 2006: Robust responses of the hydrological cycle to global warming. *J. Climate*, **19**, 5686–5699, https://doi.org/10.1175/JCLI3990.1.

Hoskins, B. J., and T. Ambrizzi, 1993: Rossby wave propagation on a realistic longitudinally varying flow. *J. Atmos. Sci.*, **50**, 1661–1671, https://doi.org/10.1175/1520-0469(1993)050<1661:RWPOAR>2.0.CO;2.

Huang, H.-P., 1999: Scale-dependent properties of optimal perturbations on a zonally varying barotropic flow. *J. Atmos. Sci.*, **56**, 1238–1247, https://doi.org/10.1175/1520-0469(1999)056<1238:SDPOOP>2.0.CO;2.

Infanti, J. M., and B. P. Kirtman, 2016: North American rainfall and temperature prediction response to the diversity of ENSO. *Climate Dyn.*, **46**, 3007–3023, https://doi.org/10.1007/s00382-015-2749-0.

Jaeger, E. B., and S. I. Seneviratne, 2011: Impact of soil moisture–atmosphere coupling on European climate extremes and trends in a regional climate model. *Climate Dyn.*, **36**, 1919–1939, https://doi.org/10.1007/s00382-010-0780-8.

Kalnay, E., and Coauthors, 1996: The NCEP/NCAR 40-Year Reanalysis Project. *Bull. Amer. Meteor. Soc.*, **77**, 437–471,

https://doi.org/10.1175/1520-0477(1996)077<0437:TNYRP>2.0.CO;2.

Kornhuber, K., S. Osprey, D. Coumou, S. Petri, V. Petoukhov, S. Rahmstorf, and L. Gray, 2019: Extreme weather events in early summer 2018 connected by a recurrent hemispheric wave-7 pattern. *Environ. Res. Lett.*, **14**, 054002, https://doi.org/10.1088/1748-9326/ab13bf.

Lee, W., and M. Mak, 1995: Dynamics of storm tracks: A linear instability perspective. *J. Atmos. Sci.*, **52**, 697–723, https://doi.org/10.1175/1520-0469(1995)052<0697:DOSTAL>2.0.CO;2.

Lehmann, J., and D. Coumou, 2015: The influence of mid-latitude storm tracks on hot, cold, dry and wet extremes. *Sci. Rep.*, **5**, 17491, https://doi.org/10.1038/srep17491.

——, ——, and K. Frieler, 2015: Increased record-breaking precipitation events under global warming. *Climatic Change*, **132**, 501–515, https://doi.org/10.1007/s10584-015-1434-y.

——, F. Mempel, and D. Coumou, 2018: Increased occurrence of record-wet and record-dry months reflect changes in mean rainfall. *Geophys. Res. Lett.*, **45**, 13 468–13 476, https://doi.org/10.1029/2018GL079439.

Li, R. C., W. Zhou, and T. Li, 2014: Influences of the Pacific–Japan teleconnection pattern on synoptic-scale variability in the western North Pacific. *J. Climate*, **27**, 140–154, https://doi.org/10.1175/JCLI-D-13-00183.1.

Li, Y., D. W. J. Thompson, and S. Bony, 2015: The influence of atmospheric cloud radiative effects on the large-scale atmospheric circulation. *J. Climate*, **28**, 7263–7278, https://doi.org/10.1175/JCLI-D-14-00825.1.

Lin, M., and P. Huybers, 2016: Revisiting whether recent surface temperature trends agree with the CMIP5 ensemble. *J. Climate*, **29**, 8673–8687, https://doi.org/10.1175/JCLI-D-16-0123.1.

Lorenz, R., E. B. Jaeger, and S. I. Seneviratne, 2010: Persistence of heat waves and its link to soil moisture memory. *Geophys. Res. Lett.*, **37**, L09703, https://doi.org/10.1029/2010GL042764.

Mak, M., 2011a: Chapter 6.8: Influences of the Earth's sphericity in the QG theory. *Atmospheric Dynamics*, Cambridge Press, 182–186.

——, 2011b: Chapter 8B.3: Optimal growth of barotropic disturbance. *Atmospheric Dynamics*, Cambridge Press, 235–240.

——, and M. Cai, 1989: Local barotropic instability. *J. Atmos. Sci.*, **46**, 3289–3311, https://doi.org/10.1175/1520-0469(1989)046<3289:LBI>2.0.CO;2.

McCrary, R. R., D. A. Randall, and C. Stan, 2014: Simulations of the West African monsoon with a superparameterized climate model. Part II: African easterly waves. *J. Climate*, **27**, 8323–8341, https://doi.org/10.1175/JCLI-D-13-00677.1.

Mills, C. M., and J. E. Walsh, 2013: Seasonal variation and spatial patterns of the atmospheric component of the Pacific decadal oscillation. *J. Climate*, **26**, 1575–1594, https://doi.org/10.1175/JCLI-D-12-00264.1.

Mitas, C. M., and W. A. Robinson, 2005: Atmospheric stability in a generalized barotropic model. *J. Atmos. Sci.*, **62**, 476–491, https://doi.org/10.1175/JAS-3375.1.

Myoung, B., and J. W. Nielsen-Gammon, 2010: The convective instability pathway to warm season drought in Texas. Part I: The role of convective inhibition and its modulation by soil moisture. *J. Climate*, **23**, 4461–4473, https://doi.org/10.1175/2010JCLI2946.1.

Newman, M., M. A. Alexander, and J. D. Scott, 2011: An empirical model of tropical ocean dynamics. *Climate Dyn.*, **37**, 1823–1841, https://doi.org/10.1007/s00382-011-1034-0.

Nishii, K., and H. Nakamura, 2004: Lower-stratospheric Rossby wave trains in the Southern Hemisphere: A case-study for late winter of 1997. *Quart. J. Roy. Meteor. Soc.*, **130**, 325–345, https://doi.org/10.1256/qj.02.156.

Petoukhov, V., S. Petri, S. Rahmstorf, D. Coumou, K. Kornhuber, and H. J. Schellnhuber, 2016: Role of quasi-resonant planetary wave dynamics in recent boreal spring-to-autumn extreme events. *Proc. Natl. Acad. Sci. USA*, **113**, 6862–6867, https://doi.org/10.1073/pnas.1606300113.

Pfleiderer, P., and D. Coumou, 2018: Quantification of temperature persistence over the Northern Hemisphere land-area. *Climate Dyn.*, **51**, 627–637, https://doi.org/10.1007/s00382-017-3945-x.

Rayner, N. A., D. E. Parker, E. B. Horton, C. K. Folland, L. V. Alexander, D. P. Rowell, E. C. Kent, and A. Kaplan, 2003: Global analyses of sea surface temperature, sea ice, and night marine air temperature since the late nineteenth century. *J. Geophys. Res.*, **108**, 4407, https://doi.org/10.1029/2002JD002670.

Russell, D. R., 2006: Development of a time-domain, variable-period surface-wave magnitude measurement procedure for application at regional and teleseismic distances. Part I: Theory. *Bull. Seismol. Soc. Amer.*, **96**, 665–677, https://doi.org/10.1785/0120050055.

Seager, R., N. Naik, M. Ting, M. A. Cane, N. Harnik, and Y. Kushnir, 2010: Adjustment of the atmospheric circulation to tropical Pacific SST anomalies: Variability of transient eddy propagation in the Pacific–North America sector. *Quart. J. Roy. Meteor. Soc.*, **136**, 277–296, https://doi.org/10.1002/qj.588.

Simmons, A. J., M. Wallace, and G. W. Branstator, 1983: Barotropic wave propagation and instability, and atmospheric teleconnection patterns. *J. Atmos. Sci.*, **40**, 1363–1392, https://doi.org/10.1175/1520-0469(1983)040<1363:BWPAIA>2.0.CO;2.

Stevens, M. R., and G. J. Hakim, 2005: Perturbation growth in baroclinic waves. *J. Atmos. Sci.*, **62**, 2847–2863, https://doi.org/10.1175/JAS3502.1.

Stolpe, M. B., I. Medhaug, and R. Knutti, 2017: Contribution of Atlantic and Pacific multidecadal variability to twentieth-century temperature changes. *J. Climate*, **30**, 6279–6295, https://doi.org/10.1175/JCLI-D-16-0803.1.

Teng, H., G. Branstator, H. Wang, G. Meehl, and W. Washington, 2013: Probability of US heat waves affected by a subseasonal planetary wave pattern. *Nat. Geosci.*, **6**, 1056–1061, https://doi.org/10.1038/ngeo1988.

Thorne, P., S. Outten, I. Bethke, and O. Seland, 2015: Investigating the recent apparent hiatus in surface temperature increases: 2. Comparison of model ensembles to observations. *J. Geophys. Res. Atmos.*, **120**, 8597–8620, https://doi.org/10.1002/2014JD022805.

Vimont, D. J., M. A. Alexander, and M. Newman, 2014: Optimal growth of central and east Pacific ENSO events. *Geophys. Res. Lett.*, **41**, 4027–4034, https://doi.org/10.1002/2014GL059997.

Wang, H., B. Wang, F. Huang, Q. Ding, and J.-Y. Lee, 2012: Interdecadal changes of the boreal summer circumglobal teleconnection (1958–2010). *Geophys. Res. Lett.*, **39**, L12704, https://doi.org/10.1029/2012GL052371.

Webster, P. J., G. J. Holland, J. A. Curry, and H.-R. Chang, 2005: Changes in tropical cyclone number, duration, and intensity in a warming environment. *Science*, **309**, 1844–1846, https://doi.org/10.1126/science.1116448.

Westra, S., L. V. Alexander, and F. W. Zwiers, 2013: Global increasing trends in annual maximum daily precipitation.

J. Climate, **26**, 3904–3918, https://doi.org/10.1175/JCLI-D-12-00502.1.

Williams, A. P., R. Seager, J. T. Abatzoglou, B. I. Cook, J. E. Smerdon, and E. R. Cook, 2015: Contribution of anthropogenic warming to California drought during 2012–2014. *Geophys. Res. Lett.*, **42**, 6819–6828, https://doi.org/10.1002/2015GL064924.

Wolfe, C. L., and R. M. Samelson, 2008: Singular vectors and time-dependent normal modes of a baroclinic wave-mean oscillation. *J. Atmos. Sci.*, **65**, 875–894, https://doi.org/10.1175/2007JAS2364.1.

Xie, S.-P., and Coauthors, 2015: Towards predictive understanding of regional climate change. *Nat. Climate Change*, **5**, 921–930, https://doi.org/10.1038/nclimate2689.

Zhang, Y., and I. M. Held, 1999: A linear stochastic model of a GCM's midlatitude storm tracks. *J. Atmos. Sci.*, **56**, 3416–3435, https://doi.org/10.1175/1520-0469(1999)056<3416:ALSMOA>2.0.CO;2.

Zhao, S., Y. Deng, and R. X. Black, 2016: Warm season dry spells in the central and eastern United States: Diverging skill in climate model representation. *J. Climate*, **29**, 5617–5624, https://doi.org/10.1175/JCLI-D-16-0321.1.

——, ——, and ——, 2017a: A dynamical and statistical characterization of U.S. extreme precipitation events and their associated large-scale meteorological patterns. *J. Climate*, **30**, 1307–1326, https://doi.org/10.1175/JCLI-D-15-0910.1.

——, ——, and ——, 2017b: Observed and simulated spring and summer dryness in the United States: The impact of the Pacific sea surface temperature and beyond. *J. Geophys. Res. Atmos.*, **122**, 12 713–12 731, https://doi.org/10.1002/2017JD027279.

——, ——, and ——, 2018: An intraseasonal mode of atmospheric variability relevant to the U.S. hydroclimate in boreal summer: Dynamic origin and East Asia connection. *J. Climate*, **31**, 9855–9868, https://doi.org/10.1175/JCLI-D-18-0206.1.

Zhu, Z., and T. Li, 2016: A new paradigm for continental U.S. summer rainfall variability: Asia–North America teleconnection. *J. Climate*, **29**, 7313–7327, https://doi.org/10.1175/JCLI-D-16-0137.1.